PTEP

Prog. Theor. Exp. Phys. **2021** 123H02(12 pages)
DOI: 10.1093/ptep/ptab148

Performance of an emulsion telescope for gamma-ray observations in the GRAINE2018 balloon-borne experiment

Yuya Nakamura[1,*], Shigeki Aoki[2], Atsushi Iyono[3], Ayaka Karasuno[2], Kohichi Kodama[4], Ryosuke Komatani[1], Masahiro Komatsu[1], Masahiro Komiyama[1], Kenji Kuretsubo[2], Toshitsugu Marushima[2], Syota Matsuda[2], Kunihiro Morishima[1], Misaki Morishita[1], Naotaka Naganawa[1], Mitsuhiro Nakamura[1,5], Motoya Nakamura[2], Takafumi Nakamura[2], Noboru Nakano[1], Toshiyuki Nakano[1,5], Akira Nishio[1], Miyuki Oda[2], Hiroki Rokujo[1], Osamu Sato[1], Kou Sugimura[1], Atsumu Suzuki[2], Satoru Takahashi[2], Mayu Torii[1], Saya Yamamoto[3], and Masahiro Yoshimoto[6]

[1]*Nagoya University, Nagoya 464-8602, Japan*
[2]*Kobe University, Kobe 657-8501, Japan*
[3]*Okayama University of Science, Okayama 700-0005, Japan*
[4]*Aichi University of Education, Kariya 448-8542, Japan*
[5]*Kobayashi-Maskawa Institute for the Origin of Particles and the Universe, Nagoya University, Nagoya 464-8602, Japan*
[6]*Gifu University, Gifu 501-1193, Japan*
*E-mail: ynakamura@flab.phys.nagoya-u.ac.jp

Received July 26, 2021; Revised November 9, 2021; Accepted November 12, 2021; Published November 17, 2021

The Gamma-Ray Astro-Imager with Nuclear Emulsion (GRAINE) project is aimed at the precise observation of astronomical gamma-ray sources in the energy range of 10 MeV–100 GeV using a balloon-borne telescope utilizing a nuclear emulsion, which can help realize precise imaging with high angular resolution (1.0° at 100 MeV), polarization sensitivity, and large aperture area (10 m^2). In 2018, the third balloon experiment was carried out as a demonstration of the detection of the brightest known astronomical gamma-ray source, the Vela pulsar, with an aperture area of 0.38 m^2. In these data, some gamma rays were produced by the $\pi^0 \to 2\gamma$ decay, which was caused by the hadronic interactions of cosmic rays in the detector. These could be used to calibrate the reconstructed angle, energy, and so on. In this study, we establish a method of searching for hadronic interactions and concomitant gamma rays with high statistics and purity. Our analysis indicates that the performance of our detector for gamma rays is as expected in wide incidence angle and energy ranges. We plan to commence scientific observations using the proposed system with the verified high angular resolution and largest aperture area in 2022 or later.

Subject Index F10, H22

1. Introduction

The observation of cosmic gamma rays is crucial for understanding high-energy astrophysical phenomena. The knowledge obtained in the past through such observations has been useful in various fields. The Large Area Telescope on the *Fermi Gamma-ray Space Telescope* (*Fermi*-LAT) launched in 2008 was used to survey the sub-GeV/GeV gamma-ray sky [1]. Significant

results such as the discovery of the acceleration of the cosmic ray proton were reported [2]. Furthermore, a combined analysis using gravitational waves and high-energy neutrinos recently led to new insights [3,4], making the observation of cosmic gamma rays even more significant. However, the observations made using the *Fermi*-LAT are limited by its angular resolution. The observations of the Galactic Center or plane region, which contains many gamma-ray sources and diffuse emissions, may suffer from particularly large systematic errors. Thus, observations with higher angular resolution are required to implement the next step of gamma-ray astronomy.

The Gamma-Ray Astro-Imager with Nuclear Emulsion (GRAINE) project pertains to the precise observation of cosmic gamma rays in the 10 MeV–100 GeV region using a balloon-borne telescope with a nuclear emulsion chamber [5]. A nuclear emulsion is a 3D tracking detector with submicron spatial resolution. It can precisely determine the arrival directions of gamma rays by measuring the electron and positron tracks produced in pair production (γ (Z or e^-) $\rightarrow e^+e^-$ (Z or e^-) where Z is a nucleus) immediately below the conversion point. The angular resolutions obtained using the nuclear emulsion film for gamma rays are 1.0° at 100 MeV and 0.1° at 1 GeV, which are approximately an order of magnitude higher than those obtained using the *Fermi*-LAT. The nuclear emulsion film is highly sensitive to gamma-ray polarization too because it can measure the azimuthal angle of the plane in which the electron and positron tracks lie; it is not affected much by multiple Coulomb scattering. Furthermore, the nuclear emulsion film can expand the aperture area without affecting the resolution, and the GRAINE project plans to observe with an aperture area of 10 m^2 repeatedly. Such an observation with a high angular resolution and a large aperture area is expected to help address the problem of unexpected GeV gamma-ray excess in the Galactic Center region [6], aid in obtaining the first result for polarization observation of a pulsar in a high-energy region, and facilitate the study of transient events with short time durations ($\leq$100 s).

So far, in the GRAINE project, the detector has been developed and balloon experiments have been conducted repeatedly. The angular resolution and polarization sensitivity of the nuclear emulsion film was demonstrated through beam experiments [7,8]. The feasibility of the observations made using the emulsion gamma-ray telescope was verified through observations made at the ground and mountain levels [7]. We also conducted three balloon experiments. The first balloon experiment (GRAINE2011) was conducted in Japan using a small-scale telescope with an aperture area of 0.013 m^2 for verifying the concept [9,10]. The second one (GRAINE2015) was performed in Australia using a middle-scale telescope with an aperture area of 0.38 m^2 for the demonstration of flight performance [11–13]. The latest one is GRAINE2018, performed in Australia, in which the brightest known gamma-ray source, the Vela pulsar, was clearly detected and the emulsion gamma-ray telescope with the highest angular resolution in this energy region was established [14].

The nuclear emulsion records the tracks for all the charged particles; cosmic rays (such as protons and helium nuclei) enter the detector during the observation. Some cause hadronic interactions and produce π^0 particles in the detector, and each π^0 immediately decays into two gamma rays. These gamma rays can be used to calibrate the arrival direction, energy, polarization, efficiency, and so on in the flight data. This analysis of the hadronic interaction has more statistics in contrast with that of a limited number of gamma rays from a celestial source; furthermore, hadronic interactions and the flux of cosmic rays are well known. Therefore, the performance of the detector, including the systematic error, can be evaluated in wide incidence

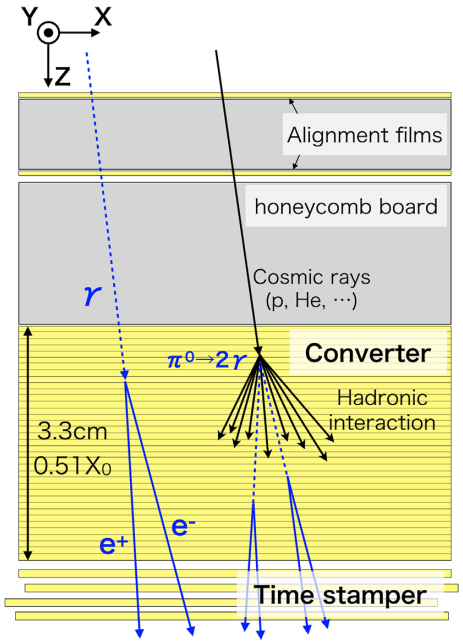

Fig. 1. Cross-sectional view of the emulsion chamber used in GRAINE2018.

angle and energy ranges using the flight data. We attempted this analysis for full-scale data for the first time in GRAINE2018. In this study, we illustrate the method of analysis used to search for hadronic interaction events and match the concomitant gamma rays and the performance of the direction and energy measurements. Furthermore, we demonstrate a new high-precision measurement system that is under development, which may help improve the angular resolution, and show the expected performance.

2. GRAINE2018 experiment

2.1 *Experimental apparatus*

An emulsion gamma-ray telescope consists of an emulsion chamber and a star camera for the attitude monitor. Figure 1 presents a cross-sectional view of the emulsion chamber. Gamma rays enter the emulsion chamber and get converted into electrons and positrons in the converter. For GRAINE2018, the converter consisted of 100 emulsion films, each composed of a 180-μm-thick plastic film and 75-μm-thick emulsion layers (measuring $25 \times 38\,\mathrm{cm}^2$) applied on both sides. The total amount of substance ($7.37\,\mathrm{g/cm}^2$) corresponds to 51% of the radiation length, 33% of the gamma-ray interaction length, and 6.6% of the nuclear interaction length. The time stamper recorded the arrival time of each track using a multistage shifter [15]. For GRAINE2018, three shifting stages were used and each time resolution is 40 min, 150 s, and ≤ 1 s. The star camera recorded the attitude of the telescope during the observation. Therefore, each event could be mapped in terms of celestial coordinates by combining the direction, time, and attitude information. In GRAINE2018, four emulsion chambers were deployed inside the pressure vessel gondola; the detailed specification of the gondola is described in Ref. [16], and the total aperture area was $0.38\,\mathrm{m}^2$.

2.2 *Flight and track data acquisition*

GRAINE2018 was conducted on April 26, 2018, in Alice Springs, Australia in collaboration with the JAXA scientific ballooning team. The duration of the flight was approximately 17 h

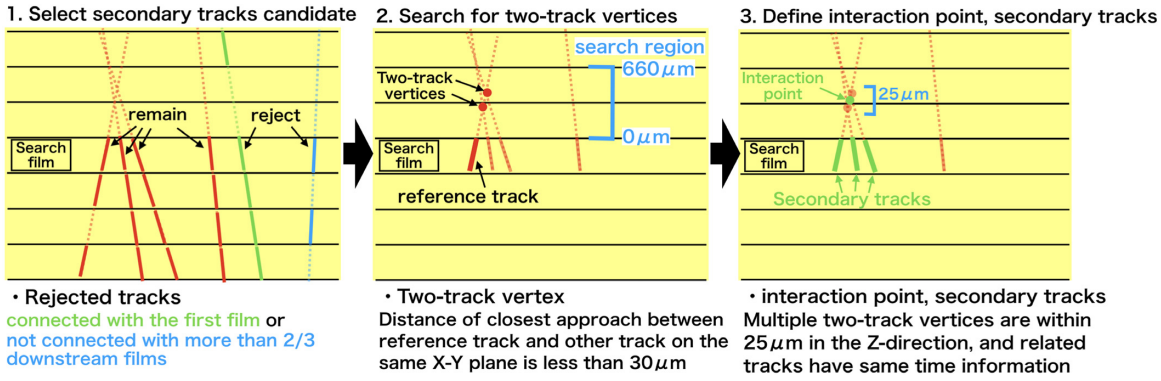

Fig. 2. Analysis flow of searching for hadronic interaction events.

and its altitude was more than 35 km (3–5 g/cm^2 of the residual atmosphere). After the emulsion films were recovered, they were developed at Sydney University and returned to Japan. We completed the readout of the tracks recorded in the films using the automatic scanning system at Nagoya University [17]. The raw data in the converter part had 1.2×10^5 tracks/cm^2, and the total scanned area was 25 cm $\times$ 38 cm $\times$ 100 films $\times$ 4 converters $=$ 38 m^2.

3. Analysis of flight data for performance evaluation

3.1 *Search for hadronic interaction events*

We searched for hadronic interaction events in the converter. Figure 2 shows an analysis flow of this. 1: Seven arbitrary and consecutive films were used in the converter. The fourth film from upstream was defined as the search film. Tracks connecting with the first film, the most upstream film, or not connecting with more than two films in three downstream films were rejected in the search film to select tracks produced in the converter. 2: The single remaining track, termed the reference track, and the other remaining tracks were extrapolated in the upstream direction (Z: 0–660 μm), and the extrapolated positions of the reference track at which the distance between the extrapolated positions of the reference track and each remaining track became minimum on the same X–Y plane were calculated. The extrapolated position accuracy is 0.2–10 μm depending on the extrapolated distance and the angle of the track. Two-track vertices of the reference track and each remaining track were defined as the extrapolated positions of the reference track when the distance of closest approach on the same X–Y plane was less than 30 μm. 3: When multiple two-track vertices were placed within 25 μm in the Z-direction and the reference track and the related tracks entered simultaneously within a time window of 40 min, they were defined as secondary tracks of one hadronic interaction event. The average of the two-track vertices was defined as the interaction point. The events were identified from all the remaining tracks as the reference track and all the films as the search film.

The distance between the interaction point and each extrapolated point of the secondary track on the same X–Y plane was defined as the degree of convergence, and it was referred to as the convergent distance. Figure 3(a) shows the average of the convergent distances for each event in one converter. The chance convergence background was estimated by extrapolating the remaining tracks in the downstream direction and searching for events using the same method. Figure 3(b) shows the number of secondary tracks when the average of the convergent distance is less than 10 μm. When the number of secondary tracks is more than three, the selected events are made to have high purity by adding the time information and requiring high convergence.

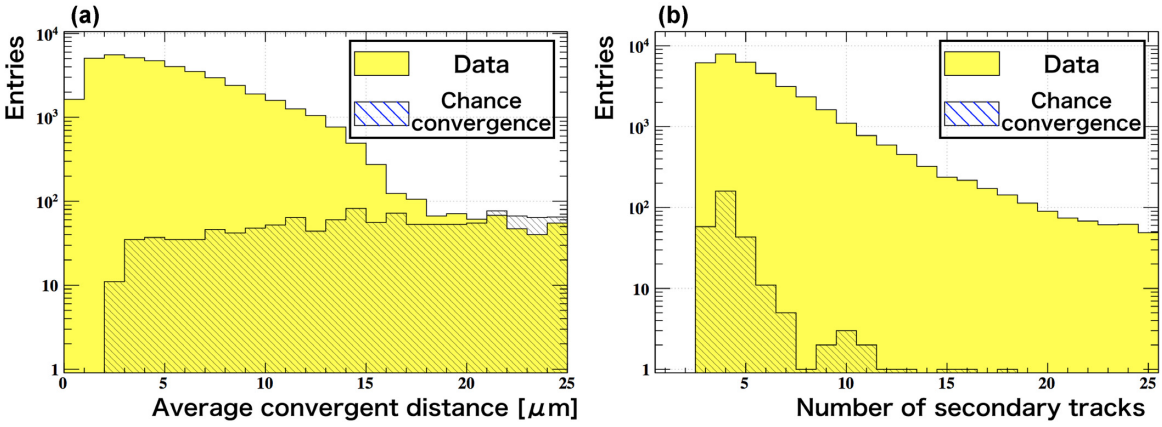

Fig. 3. (a) Distribution of the average convergent distance in one converter. (b) Distribution of the number of secondary tracks when the average convergent distance is less than 10 μm.

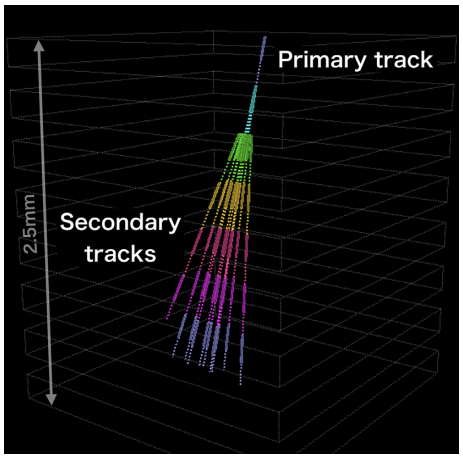

Fig. 4. Example of a hadronic interaction event detected in the converter. Each color represents a film at which the tracks are recorded.

Figure 4 shows one event, and 1.35×10^5 events were detected by searching through 100 films $\times$ 4 converters.

3.2 *Matching hadronic interactions and gamma rays*

Figure 5 shows an example of a pair production event detected in the converter. The gamma-ray direction and energy were reconstructed using the angles of the electron and positron tracks and their momenta determined using the differences in angles caused by multiple Coulomb scattering. Details of the analysis method are described in Ref. [13]. The track timestamp was processed, and 1.66×10^5 gamma-ray events were selected during the observation of the Vela pulsar; the pulsar was fully covered within 45° from the zenith for more than 6 h in a gamma-ray energy range of 100–700 MeV and an incident-angle ($\tan\theta_\gamma$) range of 0.0–1.0 (the direction of $\tan\theta_\gamma = 0$ is nearly equal to the direction of the zenith). The same time information within a time window of 40 min was provided for these events as for the hadronic interaction events; only partial timestamp information was used in this analysis, and the time resolution obtained in GRAINE2018 was 0.84 s [14]. These gamma-ray events are used in the following analysis.

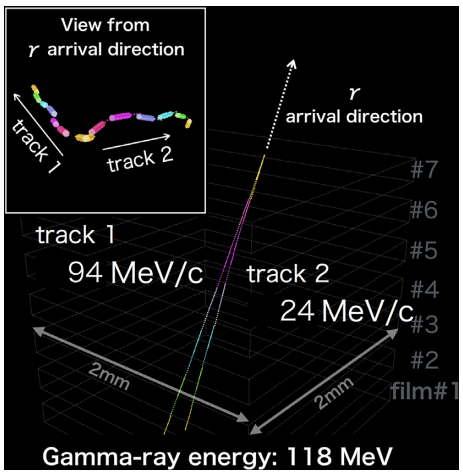

Fig. 5. An example of a pair production event detected in the converter. Each color represents a film at which the tracks were recorded.

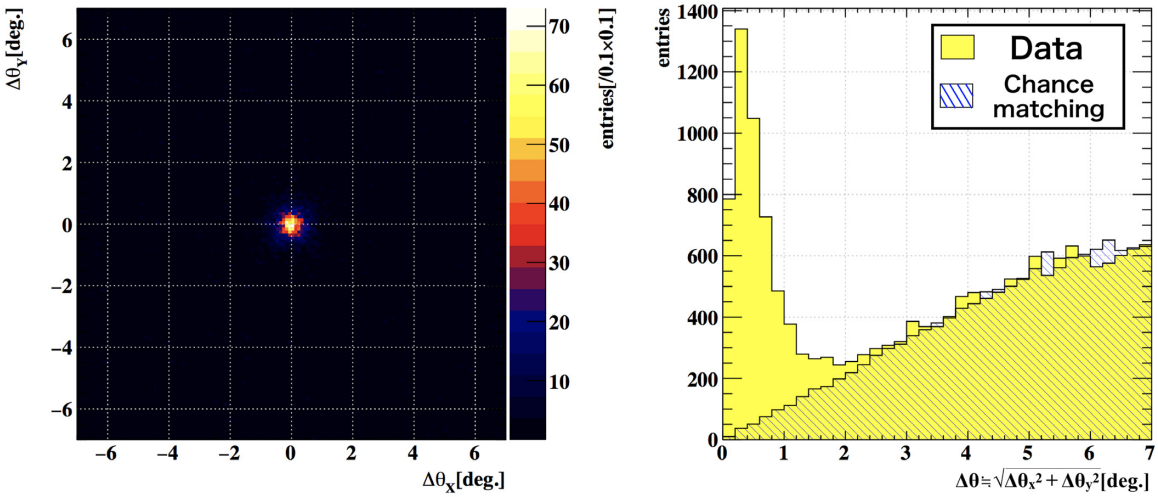

Fig. 6. Distribution of the angle difference between the expected and reconstructed gamma-ray directions.

Concomitant gamma rays with hadronic interactions were searched for in the data set. π^0 decays into two gamma rays immediately next to the interaction points. Therefore, the direction of the gamma ray via π^0 is obtained by connecting the hadronic interaction point, which is almost the same as the π^0 decay point, and the conversion point to the electron pair with the same time information. Figure 6 shows the distribution of angle difference, $\Delta\theta$, between the expected and reconstructed gamma-ray directions. The background distribution was predicted by matching using the same method after shifting only the hadronic interaction points by 1 cm. This matching and shifting was done five times in various directions on the X–Y plane. The results of the matching were normalized using the number of events lying in the interval $3^\circ \leq \Delta\theta \leq 7^\circ$. The detected gamma rays were clearly concentrated around the origin, which was the expected direction, and the total number of entries of the signal component was 8.9×10^3 events.

Figure 7 presents the distribution of the number of gamma rays matching each hadronic interaction after applying the $\Delta\theta$ cut depending on the incidence angle of the gamma rays.

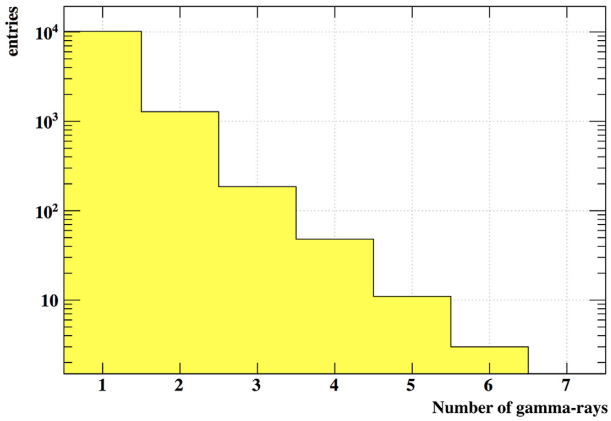

Fig. 7. Distribution of the number of gamma rays matching each hadronic interaction.

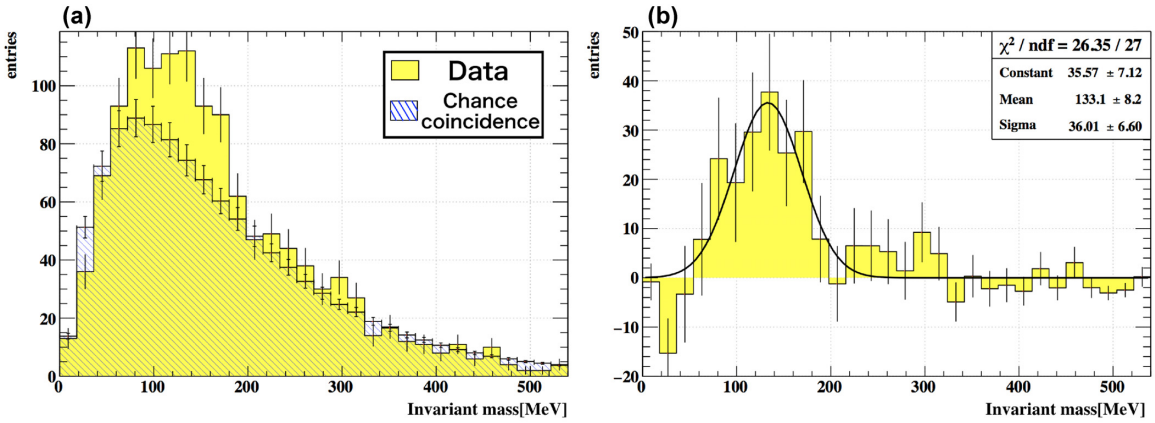

Fig. 8. (a) Invariant mass distribution of matched two gamma rays. (b) Distribution of the data subtracting the chance coincidence background and the Gaussian fitted curve.

Certain events had more than two concomitant gamma rays and most of them were produced through different π^0 decays. However, both gamma rays produced through one π^0 decay were detected in certain events. Figure 8(a) shows the invariant mass distribution for the 1.3×10^3 events of matching the two gamma rays as shown in Fig. 7. This is calculated by $M = \sqrt{2E_1E_2(1-\cos\phi)}$ where M is the invariant mass of π^0, E_1 and E_2 are the energies of the gamma rays, and ϕ is the opening angle between two gamma rays. The chance coincidence background distribution was estimated by shuffling the energy of all the evaluated gamma rays, considering the detector response for the incidence angle, and calculating the invariant mass distribution 1000 times. Thereafter, the distribution was normalized by the number of entries in the region of energy ≥ 270 MeV; the error bars in the distribution represent the statistical errors in the normalization. Figure 8(b) presents the background-subtracted invariant mass distribution with a Gaussian fitted curve. The mean value of the Gaussian distribution was 133.1 ± 8.2 MeV and was consistent with the invariant mass of π^0 (135.0 MeV). Furthermore, the standard deviation of the distribution was 36.0 ± 6.6 MeV and the energy resolution of the gamma rays was estimated as $\sqrt{2} \times (36.0 \pm 6.6)/135.0 \simeq 37.7 \pm 6.9\%$ when the contribution from the opening angle determination is neglected. The expected energy resolution based on a simulation using the current energy reconstruction method is 30%–40%; thus, the evaluated value is consistent with it. A detailed analysis of the angular resolution of the gamma rays is

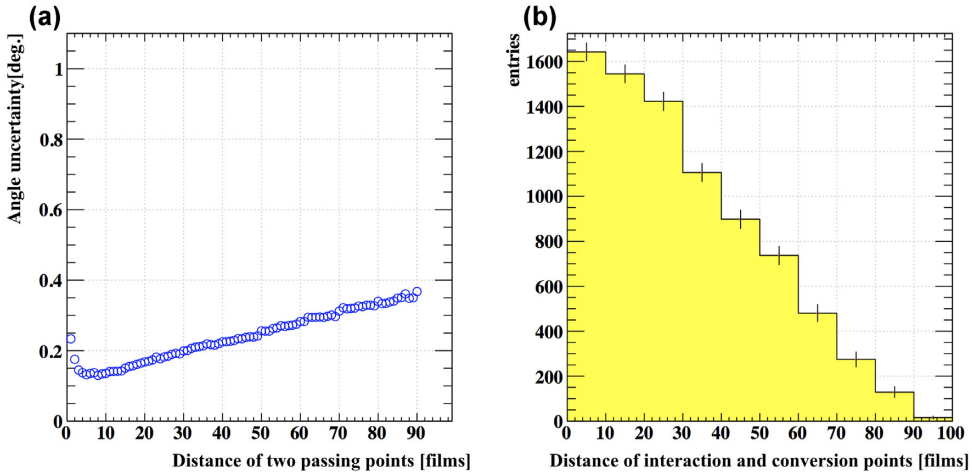

Fig. 9. (a) Distance dependence of the uncertainty of the angle determined by connecting two distant points. (b) Distribution of the distance between the films detecting the hadronic interaction and concomitant gamma rays.

given in the following section and $\delta\phi/\phi$ is about 5%, where $\delta\phi$ is the accuracy of determining the opening angle. This analysis indicates that the selected concomitant gamma rays were certainly produced through π^0 decay, and the gamma rays detected in the flight data had the expected energy resolution.

3.3 *Uncertainty of expected direction*

The angular resolution of the reconstructed gamma rays was evaluated as a radius that contains 68% of the signal component of the angle difference distribution shown in Fig. 6. However, this value included the uncertainty of the expected direction, which was to be subtracted for evaluating the performance of the observations. The uncertainty of the direction determined by connecting two distant points in the converter was estimated by evaluating the difference between the angles subtended by high-energy tracks, with negligible scattering, and the direction made by connecting two passing points. Figure 9(a) shows the distance dependence of the uncertainty. The alignment between the films was corrected using all the recorded tracks, and the accuracy depended on the distance between the corrected films. Figure 9(b) presents the distribution of distances between the film that detects the hadronic interaction and the film that detects the concomitant gamma rays. Thus, the overall uncertainty of the expected direction was estimated as the weighted average of the uncertainty shown in Fig. 9(a) and the distance between the two points shown in Fig. 9(b). Figure 9(a) indicates that the variation in the accuracy within a short distance was large. Therefore, the events in which the distance between the hadronic interaction point and the gamma-ray conversion point is more than 10 films were used for the evaluation of the angular resolution.

4. Performance of angular measurement

4.1 *Result of evaluation*

Figure 10 presents the incidence angle (θ_γ) dependence of the evaluated angular resolution for gamma rays in three energy regions (100–300, 300–500, and 500–700 MeV). The angular resolution was defined as the radius that contains 68% of the signal component in Fig. 6 after subtracting the uncertainty of the expected direction calculated for each incidence angle and

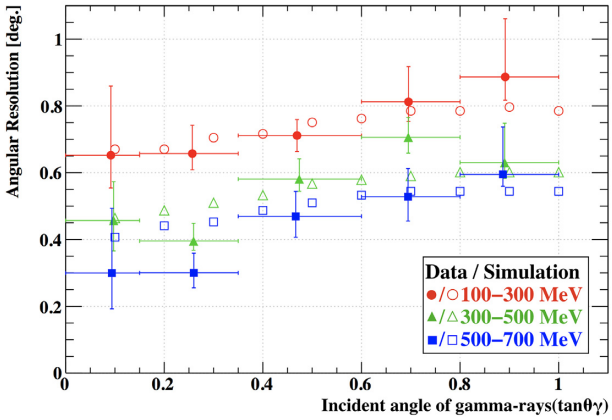

Fig. 10. Incident-angle dependence of the angular resolution for the gamma rays. The closed shapes represent the data and the open shapes represent the simulation. The circles, triangles, and squares represent the 100–300, 300–500, and 500–700 MeV energy regions for the gamma rays, respectively.

energy region. Error bars for the vertical axis represent the statistical error; those for the horizontal axis represent the incidence angle range of the evaluated gamma rays. As a standard, 20 films were used to reconstruct the momenta. Therefore, the gamma rays detected in the 19 films downstream were not used to reduce the energy migration here. The expected angular resolution was estimated through a Monte Carlo simulation using the response of the latest emulsion readout system and Geant 4.10.01 [18].

4.2 *Discussion and development for improving the performance*

The expected angular resolution shown in Fig. 10 is mostly attributed to the scattering effect (gamma rays with higher energy have a smaller effect) and the accuracy of the angular measurement for the electron pair tracks obtained using the latest high-speed emulsion readout system; insufficient position measurement accuracy in the direction of the depth causes the angular resolution for large incidence angles to deteriorate. Thus, the evaluated values were consistent with the expected ones, which were dependent on the incidence angle and energy. This result indicates that the gamma rays in the flight data demonstrated the expected performance in wide incidence angle and energy ranges during the observation.

Although the angular resolution of the gamma rays in the flight data was as expected, they were limited by the measurement accuracy of the latest high-speed emulsion readout system. The system was optimized for high-speed scanning, but it was not accurate enough to ensure the optimum performance of the emulsion film. Furthermore, the limited resolution could not clearly separate certain extremely close ($<10\,\mu$m) electron pair tracks immediately below the conversion point. This made the angular resolution of the gamma rays worse.

A high-speed scanning system was necessary to measure the enormous number of tracks recorded in the film. However, only the gamma-ray events detected by the high-speed scanning system could be reanalyzed using a microscope, which has better measurement accuracy. A high-precision manual measurement was performed for certain beam experiments and so on, and this demonstrated the measurement of gamma rays with high angular resolution and polarization sensitivity [7,8]. Thus, we developed an automatic high-precision measurement system combining the high-speed measurement system for the observations with a large aperture area. Figure 11 presents a microscopic view of the pair production event in the flight film and the

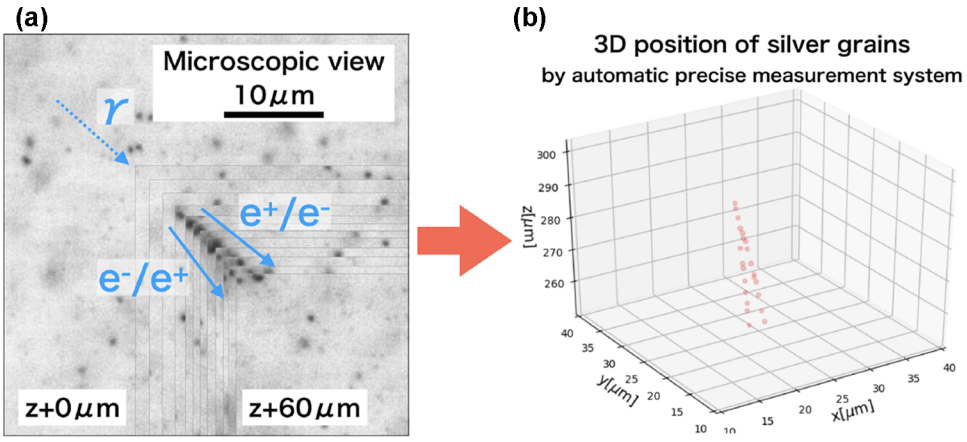

Fig. 11. (a) Microscopic view of the pair production event detected in the flight film. Tomographic images captured at intervals of 5 μm depth are overlaid. (b) 3D position of silver grains obtained using the new automatic high-precision measurement system.

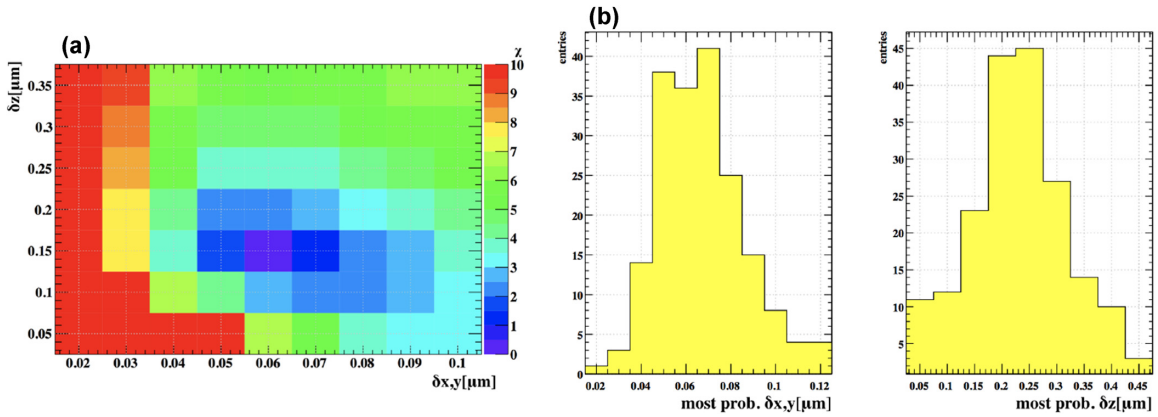

Fig. 12. (a) Probability distribution of accuracy in determining the position estimated by comparing the deviation of each silver grain from the fitted straight line for a high-energy track in the flight film with that obtained from the simulation. (b) Distribution of the most probable accuracy obtained from 189 tracks. The mean values indicate the accuracy in determining the position in the direction of the plane, $\delta_{x,y} = 0.067 \pm 0.001$ μm, and that in the direction of the depth, $\delta_z = 0.231 \pm 0.007$ μm.

3D position of the silver grains obtained using the high-precision measurement system. Figure 12 presents the results of the evaluation of the accuracy in determining the position of each silver grain that comprises the tracks. Figure 12(a) shows the probability distribution of the accuracy estimated by comparing the deviation of each silver grain from the fitted straight line for a high-energy track in the flight film with the deviation evaluated by the simulation. The high-energy track penetrates the converter from top to bottom with smaller differences in angles caused by multiple Coulomb scattering than the angular resolution of the high-speed scanning system, and the selection requirement cut 99.9% of 10 GeV proton tracks. Figure 12(b) presents the distribution of the most probable accuracy obtained from 189 tracks. The mean values indicate the accuracy in the direction of the plane, $\delta_{x,y} = 0.067 \pm 0.001$ μm, and that in direction of the depth, $\delta_z = 0.231 \pm 0.007$ μm. This value was approximately an order of magnitude smaller than that attained by the high-speed scanning systems ($\delta_{x,y} \simeq 0.4$ μm, $\delta_z \simeq 2.0$ μm). Figure 13 presents the expected angular resolution for gamma rays obtained using the Monte Carlo

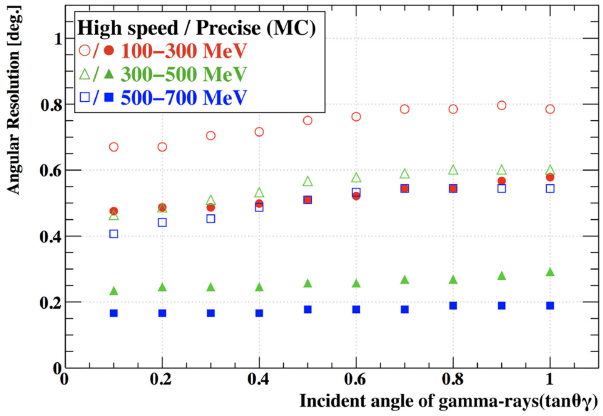

Fig. 13. Expected angular resolution obtained using the new high-precision measurement system. The open shapes represent the resolution simulated with the accuracy of the high-speed scanning system, and the closed shapes represent that of the high-precision measurement system. The circles, triangles, and squares represent the 100–300, 300–500, and 500–700 MeV energy regions of the gamma rays, respectively.

simulation with the above-mentioned accuracy; the value was approximately 1.5–3 times better than that obtained using the high-speed scanning system. Furthermore, recorded tracks could be detected in the form of a series of silver grains through the high-precision measurement, in contrast to detecting them as straight lines through high-speed scanning. Thus, the angular resolution can be further improved compared to that shown in Fig. 13 with the realization of measurements with lower scattering, and we expect to be able to measure the polarization of high-energy gamma rays.

5. Summary and prospects

We have described the GRAINE project, which is a precise cosmic gamma-ray observation project in the 10 MeV–100 GeV energy region using a nuclear emulsion chamber. The third balloon experiment, GRAINE2018, was conducted for the demonstration of the overall performance through detection of the Vela pulsar with an aperture area of 0.38 m^2, and succeeded in the detection with the highest angular resolution in this energy region [14].

The detailed performance of GRAINE2018 was evaluated using the flight data. Hadronic interactions were selected with high purity in the converter part to use the time and convergence information of the secondary tracks. Gamma rays produced by π^0 decay were selected by comparing the detected direction of the gamma rays with the expected direction, which is calculated by connecting the hadronic interaction points and the conversion points of the gamma rays. The reliability of the selection was tested by calculating the distribution of the invariant masses of gamma-ray pairs, which was consistent with the invariant mass of π^0, and the resolution was consistent with the simulated energy resolution of the gamma rays. Thereafter, the angular resolution was evaluated using the selected gamma rays with careful estimation of the uncertainty of the expected direction, which was consistent with the simulated values in wide incidence angle and energy ranges. Thus we have established an evaluation method using the gamma rays produced from hadronic interactions in the balloon-borne experiment with high credibility and confirmed that the gamma rays detected in GRAINE2018 performed as expected. Furthermore, we have developed an automatic high-precision measurement system

and demonstrated that it has an accuracy that is approximately an order of magnitude higher than that of the high-speed scanning system. If applied to gamma-ray events, this system will produce an angular resolution that is more than 1.5–3 times better than the value evaluated through the analysis of the hadronic interactions. In addition, the first observation with polarization sensitivity will be performed in this energy region.

We plan to commence scientific observations in 2022 or later, and the next balloon experiment with an aperture area of 2.5 m^2 will be conducted twice in 2022 by JAXA in Australia. The aims are to realize the largest aperture area in this energy region, to capture a high-resolution image in the GeV region for the Vela pulsar, to begin the first polarization measurement in the pair production mode, and to observe the Galactic Center region.

Acknowledgments

The balloon-borne experiment was conducted by the Scientific Ballooning (DAIKIKYU) Research and Operation Group, ISAS, JAXA (PI support: C. Ikeda) with CSIRO. English proofreading of this manuscript was done by a professional editor. This work was supported by JSPS KAKENHI (grant numbers 17H06132, 18H01228, and 18K13562).

References

[1] S. Abdollahi et al., Astrophys. J. Suppl. Ser. **247**, 33 (2020).
[2] M. Ackermann et al., Science **339**, 807 (2013).
[3] B. P. Abbott et al., Astrophys. J. Lett. **848**, (2017).
[4] The IceCube Collaboration et al., Science **361**, eaat1378 (2018).
[5] S. Takahashi et al., Adv. Space Res. **62**, 2945 (2018).
[6] T. Daylan et al., Phys. Dark Universe **12**, 1 (2016).
[7] S. Takahashi, PhD Thesis, Nagoya University (2011) [in Japanese].
[8] K. Ozaki et al., Nucl. Instrum. Meth. A **833**, 165 (2016).
[9] S. Takahashi et al., Prog. Theor. Exp. Phys. **2015**, 043H01 (2015).
[10] H. Rokujo et al., Nucl. Instrum. Meth. A **701**, 127 (2013).
[11] S. Takahashi et al., Prog. Theor. Exp. Phys. **2016**, 073F01 (2016).
[12] K. Ozaki et al., J. Instrum. **10**, P12018 (2015).
[13] H. Rokujo et al., Prog. Theor. Exp. Phys. **2018**, 063H01 (2018).
[14] S. Takahashi et al., Prog. Theor. Exp. Phys. (submitted).
[15] S. Takahashi et al., Nucl. Instrum. Meth. A **620**, 192 (2010).
[16] H. Rokujo et al., J. Instrum. **14**, P09009 (2019).
[17] M. Yoshimoto et al., Prog. Theor. Exp. Phys. **2017**, 103H01 (2017).
[18] S. Agostinelli et al., Nucl. Instrum. Meth. A **506**, 250 (2003).